nature energy

Supplementary information

https://doi.org/10.1038/s41560-026-02129-z

A $Ni(OH)_2$ symmetric battery cell for hydroxide exchange membrane-based direct air capture of CO_2

In the format provided by the authors and unedited

Table of Contents

Figures

Table

Supplementary Discussion| Comparison of carbon capture methods

The field of carbon capture has grown in operating principles, target concentrations, and application scopes. A common set of performance metrics is desired to evaluate different systems, but the field has not yet coalesced around specific metrics and their definitions. The goal of this discussion is to demonstrate low energy cost of the nickel hydroxide HEMCC technology for direct air capture (DAC), not point sources (PS). There are few demonstrated electrochemical devices conducting DAC in literature. Many technologies target point source capture and may extrapolate performance capabilities from material properties or conditions that don't represent carbon capture in practice.

Below is a table representing a scope of technologies, both electrochemical and thermal swing. Types of electrochemical carbon capture are categorically broken into pH, redox-active (RA), and electrochemically mediated amine reduction (EMAR). Technology names are based either on the capture material or style of capture depending on the developer. Concentration is split between DAC, generally 400ppm$_{CO2}$, and PS, generally 10-15%. Some technologies, specifically bipolar membrane electrodialysis BPMED, show release energies from a simulated liquid stream of dissolved carbonate or bicarbonate materials, often the capture of CO_2 into that liquid stream is not discussed making direct relation to DAC and PS technologies difficult.

The thermal swing adsorption technologies shown include the state-of-the-art technologies from CarbonEngineering and Climeworks. Two other groups are represented with proposed materials for carbon capture. First a solid Mg/Ca rock mixture for soil and ocean sequestration with significant work discussing theoretical energy requirements of a full system. Second present physisorption compounds that have been tested for their heats of adsorption energy and selectivity to CO_2 and water. The gaps between the full-scale systems of CarbonEngineering and Climeworks with demonstrated energy costs and initial laboratory materials research with theoretical energy requirements is significant and adds to confusion when comparing technologies despite the merit of publishing at different technology readiness levels.

Supplementary Table 1 attempts to show 5 levels of scope seen in literature. The highest level is a full system including blower, CO_2 capture, CO_2 release, and compression (**BCRC**) and is present in the state-of-the-art technologies. Capture and purified release (**CR**) systems capture CO_2 from a dilute source and release the CO_2 in a purified stream ignoring the costs of blowing air and compressing CO_2. The work in the manuscript with the 5000 hr durability electrodes and the 9·300cm^2 stack would fall into this category. Capture and non-purified release (**CR***) systems capture CO_2 but the release stream is not purified. The initial lab scale work in this manuscript falls under this category. CR* systems do not release a purified stream of CO_2 which can be easier to achieve in a laboratory setting and avoids second law thermodynamic penalty for purifying CO_2. Release (**R**) technologies does not do capture and focus on the energy cost to release pure CO_2 from an already captured/concentrated stream. **(Theory)** technologies do not have an actual device that does either capture or release but focus on theoretical energy requirement**.** These are generally materials technologies that have shown the capability of capturing CO_2 and relate to laboratory measurement such as a cyclic voltammogram or heat of adsorption to an energy cost to use that material in a system.

Where appropriate, the **Supplementary Table 1** shows demonstrated energy costs; theoretical energy is shown where demonstrated energy is not reported. Electron efficiency is an important metric for electrochemical cells but not always reported equivalently. Here it is defined as the ratio of CO_2

captured (n_{CO2}) to electrons used (n_e) and is maximized at 1. Also, it is the ratio of the CO_2 flux (j) through the MEA to the amount of total charge (in mol, $\frac{I}{F}$):

$$\eta_e = \frac{n_{CO2}}{n_e} = \frac{jF}{I}$$

Current density is another important metric in that it is related to the flux in the system and thus eventual system costs. Energy does scale with current density, so it is important to compare similar current densities. Systems testing release energies generally can have higher current densities because there is less efficiency loss due to the higher solution concentrations, similarly PS is more efficient at higher current densities than DAC.

To compare DAC and PS systems a second law efficiency calculation is used as the inverse of the ratio of demonstrated energy to theoretical energy calculated from the Gibbs free energy of mixing.[1]

$$E_{min} = \Delta G_{mix} = G_{feed} - G_{products}$$

$$E_{min} = -RT \cdot \left(\sum_{feed\ f} N_f \sum_{Comp\ k} X_{f,k} \ln\left(X_{f,k}\right) - \sum_{Prod\ p} N_p \sum_{Comp\ k} X_{p,k} \ln\left(X_{p,k}\right) \right)$$

$$\eta_{2ndLaw} = \frac{E_{min}}{E_{sys}} * 100\%$$

The lowest theoretical energy cost would be an infinite bath approximation where there is no change in the air concentration while producing a pure CO_2 product. This reduces the E_{min} to the chemical potential of the CO_2 in the feed stream. The second law efficiency, η_{2ndLaw}, is defined for this case as the true minimum energy requirement for a separation of CO_2 from a dilute stream. It takes considerably more energy to capture from a source of 400 ppm_{CO2} (0.118 $MWh \cdot ton_{CO2}^{-1}$) compared with a point source of 10% (0.035 $MWh \cdot ton_{CO2}^{-1}$) or 15% (0.029 $MWh \cdot ton_{CO2}^{-1}$). Relating to the thermodynamic minimum energy requirement allows for comparison across capture concentrations.

$$E_{\mathrm{min,inf-bath}} = -RT \cdot N_f \cdot X_{f,CO2} \ln\left(X_{f,CO2}\right)$$

Highlighted in the following table, are representative of technologies in the field of carbon capture. The target concentration and tested scope as described previously are shown for each. The key figure of merit, Energy Cost is given where demonstrated while electron efficiency and current density are shown for comparison. The minimum energy requirements and the respective second law efficiency are calculated for the concentration tested.

Supplementary Table 1 |Carbon capture systems in literature focused on electrochemical DAC, PS, and Solution conditions.

Scope of research is emphasized to highlight technology maturity. BCRC--full system with Blower, CO_2 Capture and Release, and Compressor. CR--Capture and Release CO_2 from a dilute stream to a purified stream. CR*--Capture and Release without purification. R—Release from a pre captured/concentrated stream. Theory—provide theoretical energy requirements outside of a device test case and have energy costs denoted as theory.

Type for electrochemical devices are split in three categories pH, Redox-Active (RA) and Electrochemically Mediated Amine Regeneration (EMAR), Technology is a description from the author. Energy Cost, Electron Efficiency, and Current Density are commonly reported data. Second Law Eff is energy efficiency based on Minimum Energy (E_{min}).

Type	Technology	Concentration	Tested Scope	Demonstrated Energy Cost	Electron Efficiency	Current Density	*Minimum Energy (E_{min})*	Second Law Eff	Ref.	Notes
				[MWh·ton^{-1}]	*CO_2 : e^-*	*[mA·cm^2]*	*[MWh·ton^{-1}]*	*%*		
EChem pH	Ni(OH)2 HEMCC	DAC (400ppm)	CR	0.46	0.43	1	*0.118*	25.5	Fig 3.a-d	This work's durability 25cm^2 cell test
EChem pH	Ni(OH)2 HEMCC	DAC (400ppm)	CR	0.83	0.26	2	*0.118*	14.2	Fig 4.a-d	This work's scale 9·300cm^2 stack test
EChem pH	Ni(OH)2 HEMCC	DAC (400ppm)	CR*	1.15	0.25	2	*0.118*	10.2	Fig 2	This work's initial 25cm^2 laboratory test
EChem pH	PSE	DAC (400ppm)	CR*	1.26-1.89	0.20-0.50	0.5-3	*0.118*	6.2-9.3	2	Oxygen pump for pH gradient with central liquid flow for release; DAC feasibility study
EChem pH	HEMFC	DAC (400ppm)	CR*	2.35-5.53	0.16-0.41	5-20	*0.118*	2.1-5	3	Hydrogen fuel cell for pH gradient targeting high removal fraction
EChem RA	Neutral Red	DAC (400ppm)	Theory	0.41_{theory}	0.33-0.39		*0.118*		4	Redox active Neutral Red in flow cell for DAC demonstration; theoretical energy presented in SI
EChem EMAR	EMAR	PS (15%)	CR	0.25-0.50		2-12	*0.029*	5.6-11.3	5	EMAR process using ethylenediamine (EDA) with Cu/Cu^{2+}. EChem cell releases CO_2 from PS solution.
EChem pH	PSE	PS (14%)	CR*	0.95-3.79	0.44-0.48	0.5-500	*0.030*	0.8-3.1	2	Oxygen pump for pH gradient with central liquid flow for release; Main work for PS demonstration
EChem RA	Isoindigo	PS (10%)	CR*	0.80	0.80	0-2	*0.035*	4.3	6	Redox active isoindigo in charge/discharge cell demonstrating feasibility, no purification presented
EChem RA	Isoindigo	PS (1%)	CR*	1.42		0-2	*0.069*	7.3	6	Redox active isoindigo in charge/discharge cell showing lower CO2 concentration feasibility
EChem RA	Neutral Red	PS (15%)	Theory	0.22_{theory}	0.50-0.71		*0.029*		4	Redox active Neutral Red in flow cell for point source demonstration; theoretical energy in SI
EChem RA	LQ	Pure (100%)	CR*	0.26-1.65	0.73-0.92	0.4-1.4	*N/A*		7	Redox active quinone in a flow cell showing energy requirement of capture/release from pure CO_2
EChem pH	BPMED	Solution	R	1.01-3.16	0.65-0.80	5-20	*N/A*	Release	8	Electrolyzer to acidify a solution of 1 M $NaHCO_3$ and show energy to release CO_2
EChem pH	BPMED	Solution	R	0.63-2.84	0.95	5-100	*N/A*	Release	9	Electrolyzer to acidify a solution of 1 M $KHCO_3$ and show energy to release CO_2
Liq-Calcine	Carbon Engineering	DAC (600ppm)	BCRC	1.82			*0.113*	6.4	10	State of the art technology using a liquid calcium hydroxide loop and releasing CO_2 in 900 °C calciner.
Solid-Amine	Climeworks	DAC (400ppm)	BCRC	2			*0.118*	5.9	11	State of the art technology using amines on solid substrate to capture and release via temp swing.
Solid-Calcine	Thermal	DAC (400ppm)	Theory	$0.65\text{-}1.3_{theory}$			*0.118*		12	Mg/Ca rock mixture to capture $Mg(HCO_3)_2$/ $Ca(HCO_3)_2$ or $MgCO3/CaCO_3$ used in ocean or soil sequestration; theoretical energy of full process.
Physisorption	Mg-MOF-74	DAC (400ppm)	Theory	0.27_{theory}			*0.118*		13	Physisorbent shown with low heats of adsorption for CO_2 capture
Physisorption	SIFSIX-18-Ni-β	DAC (400ppm)	Theory	0.33_{theory}			*0.118*		13	Physisorbent developed with low heats of adsorption and high CO_2/H_2O selectivity

Supplementary Note 1| pH gradient carbon capture

Carbon capture devices utilizing a pH gradient are bound to a minimum ΔpH to capture CO_2 on one side and release it on another. This ΔpH can be approximated by the equilibrium of CO_2 in water solutions of different pH. A reaction scheme described in prior work of CO_2 and water with equilibrium and kinetic equations has been adapted below. [14,15] Although unused in the analysis here, diffusion data can assist in modeling CO_2 capture systems by adding aqueous transport properties. [16]

$$CO_2(aq) + H_2O \underset{k_{-1}}{\overset{k_1}{\leftrightarrow}} H_2CO_3$$
$$CO_2(aq) + OH^- \underset{k_{-2}}{\overset{k_2}{\leftrightarrow}} HCO_3^-$$
$$CO_3^{2-} + H^+ \overset{K_{a1}}{\longleftrightarrow} HCO_3^-$$
$$HCO_3^- + H^+ \overset{K_{a2}}{\longleftrightarrow} H_2CO_3$$
$$OH^- + H^+ \overset{K_W}{\longleftrightarrow} H_2O$$

A set of solubility data of CO_2 and water ionization was utilized to show the equilibrium of CO_2 in air with a water solution at different pH.[17-19] Combined with the aqueous equilibrium and kinetic data ***Supplementary* Figure *1*** below was formed for 30 °C and 1 bar. The dotted red line shows the equilibrium of gaseous CO_2 over a solution. From this we can determine the pH gradient requirement between an atmospheric CO_2 solution and a purified stream. At 400 ppm a minimum of 10.4 pH is required to capture CO_2. To release the CO_2 into a purified stream the solution must drop below 7.6 pH, thus a minimum 2.8 ΔpH gradient is required in a pH gradient device. The Nernst equation allows us to determine a minimum thermodynamic voltage requirement for CO_2 capture using an electrochemical pH gradient device of 0.17V. In practicality, the capture side outlet CO_2 concentration will determine the equilibrium pH; for instance, if 50% of the CO_2 is captured, a 200ppm CO_2 outlet will require a 3.0 ΔpH.

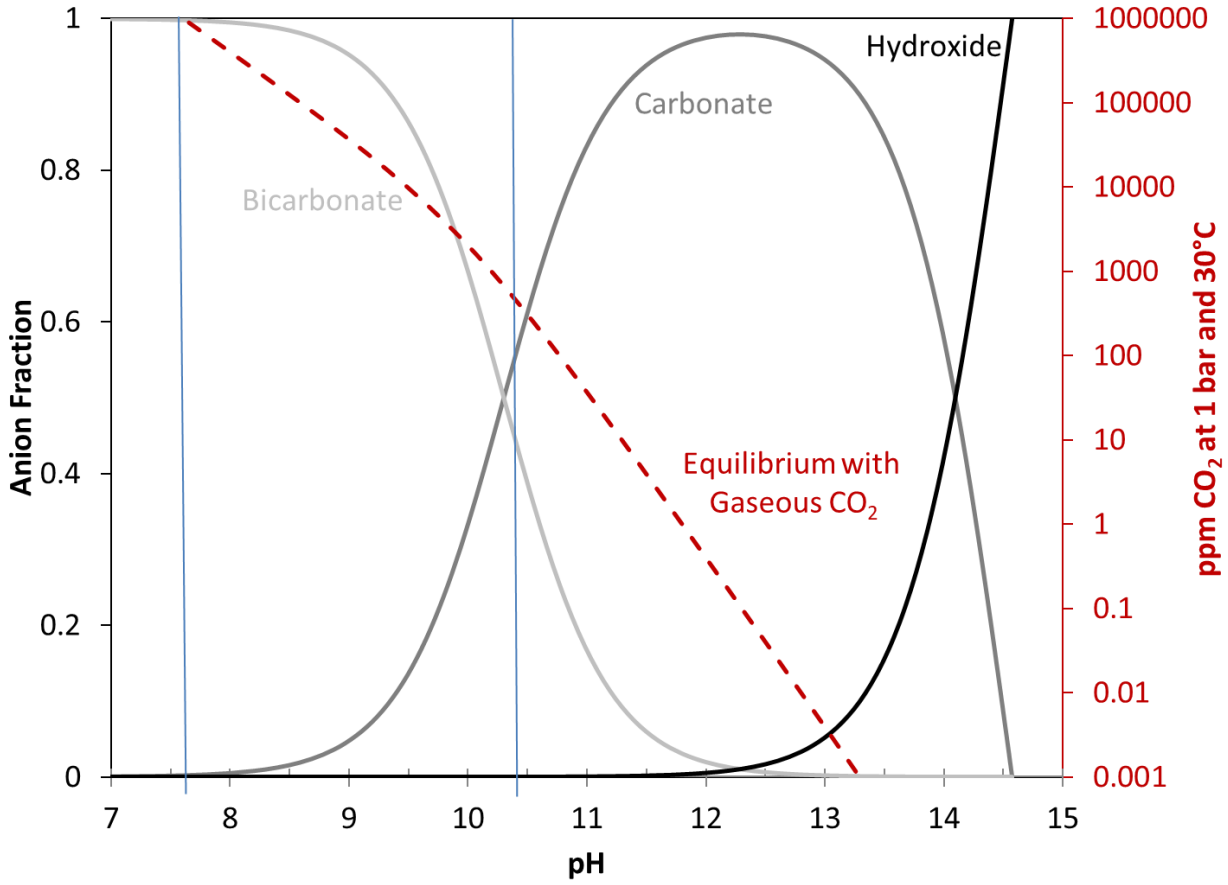

Supplementary Figure 1 | Anion aqueous solution composition in equilibrium with a CO2 in air stream at 30°C and 1 bar at varied pH.

The anion composition is a mixture of bicarbonate (light grey line), carbonate (medium grey line), and hydroxide (black line). A solution in equilibrium with a CO2 gas stream will follow the dotted red line. This can be used to determine the maximum allowable anode pH to release CO2 into a pure (1,000,000 ppm) stream and the minimum required cathode pH to capture CO2 from a dilute CO2 stream (vertical blue lines).

Supplementary Note 2| Flux and energy cost calculation

The change in mole fraction of CO_2 at cathode was monitored by Teledyne TML20 CO_2 analyzer. Instantaneous flux of CO_2 captured in the device (j) normalized to the area of MEA is defined as:

$$j\left[\frac{kg}{m^2 yr}\right] = \frac{M_{W,CO_2}\Delta y_{CO_2} PQ}{RTA}$$

Where M_{W,CO_2} is the molecular weight of CO_2, Δy_{CO_2} is the change in mole fraction of CO_2 at cathode, P is pressure, Q is the volumetric air flow rate, R is the ideal gas constant, T is temperature, and A is the electrode area.

In each specific cycle or regeneration period, the energy cost (E) normalized to the mass of CO_2 is directly dependent on the CO_2 flux given above and electric power input that is dependent on the operating voltage at constant current density:

$$E\left[\frac{MWh}{ton_{co_2}}\right] = \frac{I\int V(t)dt}{\int j(t)dt}$$

Where I is current density, V is voltage, j is the CO_2 flux, and t is time.

Voltage is commonly broken into the standards potential difference ΔE^o_{red}, kinetic overpotential η_{rxn}, ohmic loss IR_{ohm}, and Nernstian overpotential $\frac{RT}{zF} lnQ$. Residual overpotentials $\sum \eta_{resid}$ which may be related to gas transport, ion transport, or other properties like the state of charge of a battery can describe the deviations between the actual cell voltage and the other terms. The standard potential difference is 0 during the charge discharge step with $NiOOH/Ni(OH)_2$ reactions. The kinetic overpotential for batteries is low because of the quick proton exchange process that occurs in the interstitial space of the Ni-O lattice.[20]. While we did not measure this directly it is a component of the average voltage difference between the charge and discharge curves $\eta_{C/D}$ as described to be 0.09 V in **Extended Figure3c.** The ohmic loss is low due to the low current densities in the cell; R_{ohm} can be measured from the high frequency resistance of the cell and is averaged to be 4.2 Ohm·cm^2 leading to a 0.01V addition at 2 mA·cm^{-2}. The Nernstian overpotential is the predominant driving force to capture and release CO_2 and is estimated from pH gradient discussion in SI Discussion 2 to be 0.17V. In total the voltage expected during a charge/discharge step $V_{C/D}$ is expected to be 0.27 V plus any residual overpotentials.

$$V = \Delta E^o_{red} + \eta_{rxn} + IR_{ohm} - \frac{RT}{zF} lnQ + \sum \eta_{resid}$$

$$V_{C/D} = \Delta E^o_{red} + \eta_{C/D} + IR_{ohm} - \frac{RT}{zF} lnQ = 0 + 0.09 + 0.01 + 0.17 = 0.27V$$

Voltage at the end of the regeneration (V_R) can use kinetic overpotential η_{rxn} directly to describe the overpotential associated with the OER and ORR reactions. These are generally high overpotential reactions and are estimated to be 0.8 V for this cell. The voltage expected at the end of regeneration is expected to be 0.98 V plus any residual overpotentials.

$$V_R = \Delta E^o_{red} + \eta_{rxn} + IR_{ohm} - \frac{RT}{zF} lnQ = 0 + 0.8 + 0.01 + 0.17 = 0.98V$$

Supplementary Figure 2 illustrates a voltage breakdown for this system shown in **Figure 2a** during the charge/discharge step and at the end of regeneration. As discussed in the manuscript, a major focus of future work is to lower the amount of regeneration required to lower the energy costs.

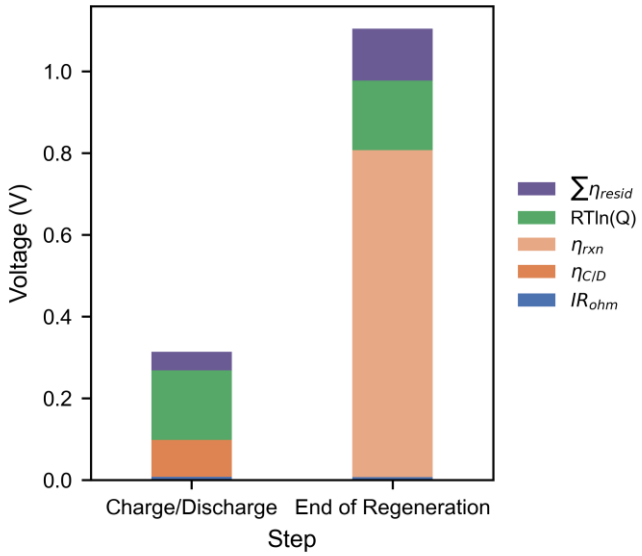

Supplementary Figure 2 | Voltage breakdown of data in Figure 2a during charge/discharge and the end of regeneration. Data is shown for the charge/discharge step and end of regeneration. For the charge/discharge step voltage contribution due to ohmic resistance IR_{ohm} measured from high frequency resistance (HFR) is 0.01V, charge/discharge voltage, $\eta_{C/D}$, is 0.09 V as measured from the ex-situ cell in **Extended Figure 3c,** pH overpotential $RTln(Q)$ is 0.17V as described **Supplementary Note 1**, the remaining overpotentials are designated as $\sum\eta_{resid}$ and are transport overpotentials outside the scope of this manuscript to measure. The residual overpotentials are estimated as the difference between the total cell voltage and the ohmic, charge/discharge voltage, and pH components. The end of regeneration is when the anode is fully charged, and OER/ORR are occurring. During this part of the cycle, the ohmic, and pH components are the same. η_{rxn} for the OER/ORR reactions are estimated to be 0.8 V but not directly measured and shown for illustration. The residual overpotentials are outside the scope of this manuscript but shown for illustration. The total energy requirements [MWh·ton$_{CO2}^{-1}$] presented throughout the manuscript include the combined effects of both the charge/discharge and regeneration steps.

Supplementary Note 3| Alternate conditions of current and CO_2 concentration in the feed

This technology focuses on DAC where low current density is required and preferred to maintain low energy costs. Traditional nickel hydroxide batteries are intended for C rates less than 1-2 C at most which lines up with the 2 mA·cm^{-2} target of this system. High C rates will lead to rapid discharge and significantly shortened cycles. **Figure 3 a-d.** shows better performance at lower current density of 1 mA·cm^{-2}. Flux tests in ***Supplementary* Figure *5***show a range regenerations from 1 to 5 mA·cm^{-2}. Below in **SI Figure 3,** a test was conducted showing cycling at 3 mA·cm^{-2}. It was conducted with an alternative regeneration scheme where several cycles were conducted below 0.6 V before regeneration. It shows how modest flux decreases occur across cycles without regeneration.

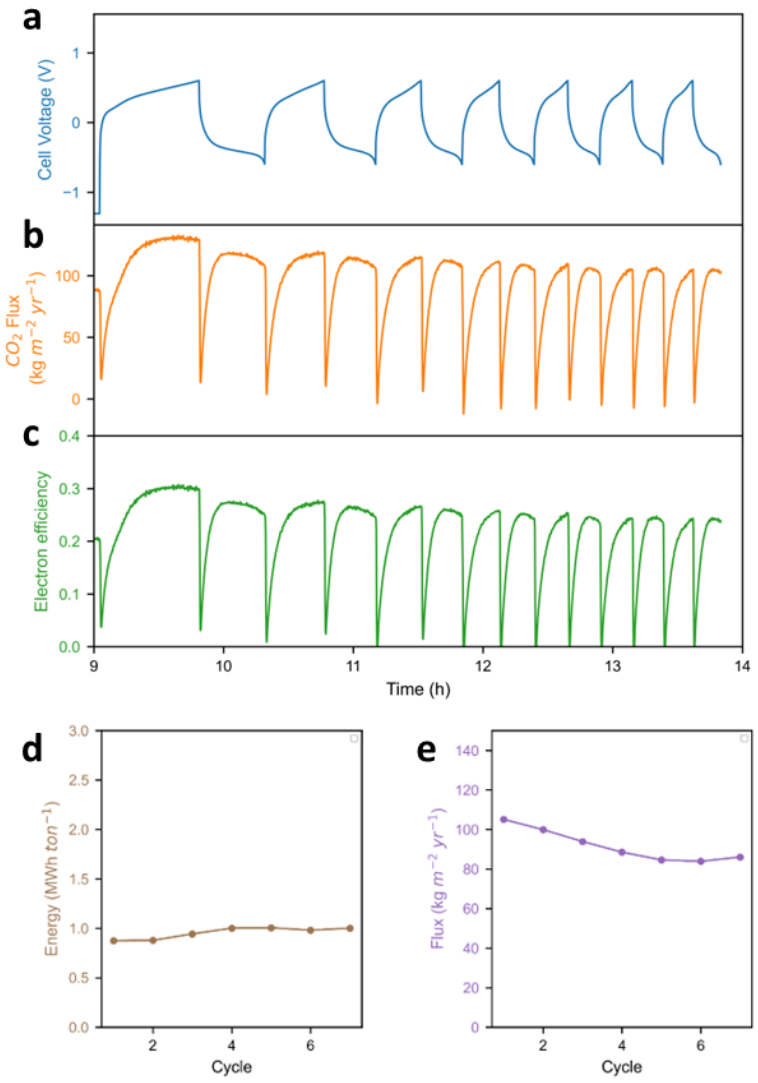

Supplementary Figure 3 | HEMCC cell at 3 mA·cm-2 and 30 °C without regeneration cycles.
Compared with the 2mA·cm^{-2} results in **Figure 2**: the **a.** cell voltage is limited to only the charge/discharge steps with limits at 0.6 V. **b.** CO_2 flux is maximized at 141 kg_{CO2}·m^{-2}·yr^{-1} modestly increased compared with 2 mA·cm^{-2} **c.** electron efficiency modestly decreased compared with 2 mA·cm^{-2} which averages to 0.24 across all cycles. **d-e.** energy and flux during cycles. Energy increases modestly across cycles while flux decreases modestly due to the lack of regeneration cycles. In this test, it is

shown we can increase current density modestly. Additionally, it highlights the need for regeneration due to modestly reduced performance across cycles

This technology, while not designed for, can work for higher CO_2 concentrations such as life support systems near 3000 ppm CO_2 and point source near 10% CO_2. To verify this, early in the research a test was ran with 1% CO_2 (10000 ppm) shown in **Supplementary Figure 4**. As expected, significantly improved flux, energy, and electron efficiency was seen compared with the DAC case. Repeats at higher concentrations were not pursued and focus was put into capabilities at DAC conditions to match the optimized C-rate of $Ni(OH)_2$ electrode.

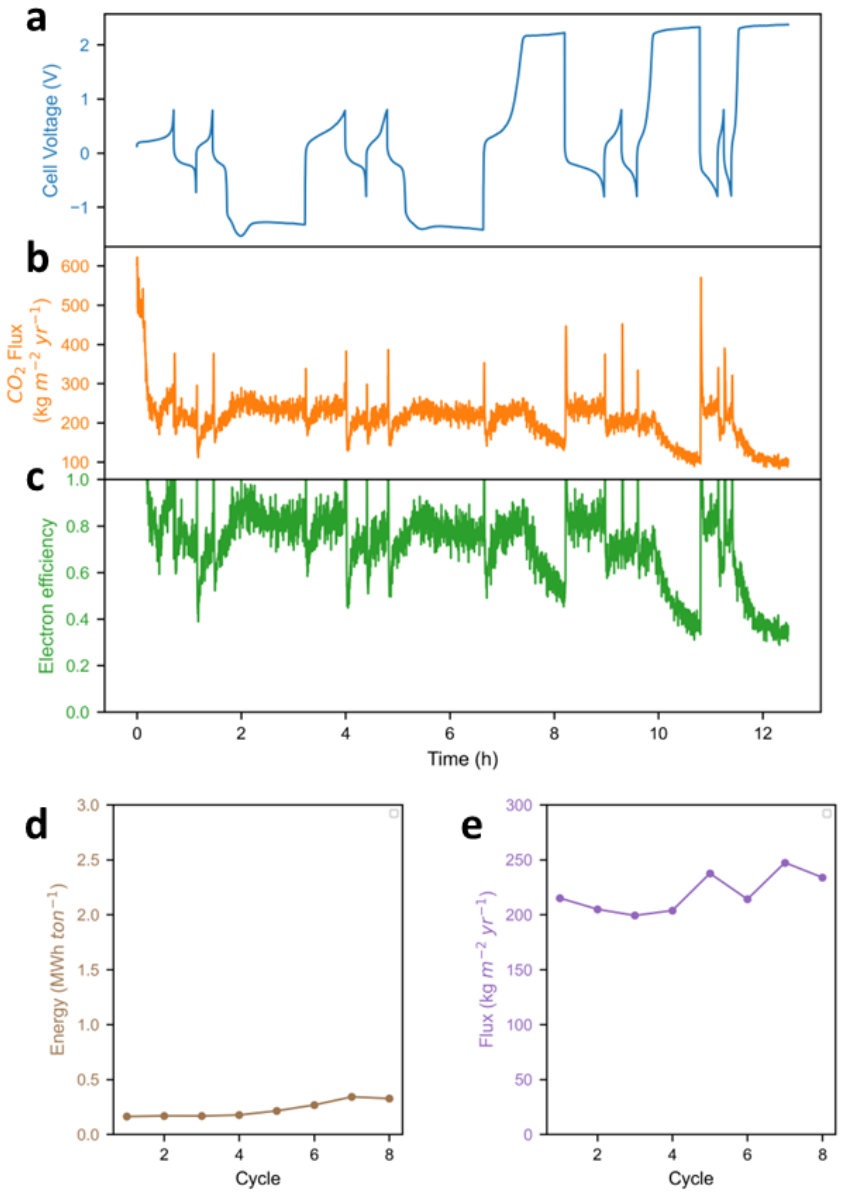

Supplementary Figure 4 | 1 L·min^{-1} of 1% (10000ppm) CO_2 in Air at 90% RH, 2 mA·cm^{-2}, and 30°C for a $Ni(OH)_2$ HEMCC cell **a.** Cell voltage with 2 charge/discharge cycles followed by an extended regeneration. The first half of the test regenerated one side and the second half regenerated the other. **b.** flux is increased to an average of 222 kg·m^{-2}·yr^{-1} and **c.** electron efficiency Is increased to an average of 0.83. The higher flux and electron efficiency is expected because of the higher CO_2 inlet

concentrations. **d-e.** Energy and flux during charge/discharge steps. The energy requirement is significantly lower because higher fluxes can be achieved from a more concentrated CO_2 source.

Supplementary Note 4| Electrochemical carbon capture limits

Electrochemical carbon capture devices have two basic and fundamental limitations that define the maximum flux at a given current density. First is stoichiometric electron efficiency, second is the mass flow into the device. This is reflect ed in prior work with a hydrogen fuel cell based HEMCC. [3] Importantly the limits can define any electrochemical system where a species is electrochemically generated to capture CO_2. In this case hydroxide is produced from water, but other systems such as quinone or isoindigo can also be described in this manner. [6,7] When a solution of CO_2 capture species is produced, the flux limits can be adjusted for solution volume instead of an area-based electrode.

Stoichiometric flux limits:

$$j_{stoic\_bicarb} = \frac{n_{bicarb}}{n_x} * \frac{n_x}{n_e} * \frac{m_{CO_2}}{F} * \frac{I}{A} = \frac{1}{1} * \frac{1}{1} * \frac{44.01}{96485} * \frac{I}{A} = C_1 \frac{I}{A};\ where\ x = OH^-$$

$$j_{stoic\_carb} = \frac{n_{carb}}{n_x} * \frac{n_x}{n_e} * \frac{m_{CO_2}}{F} * \frac{I}{A} = \frac{1}{2} * \frac{1}{1} * \frac{44.01}{96485} * \frac{I}{A} = \frac{1}{2} C_1 \frac{I}{A};\ where\ x = OH^-$$

Mass flow flux limits:

$$j_{mass\ Flow} = n_{CO_2} * C_2 \frac{Q}{A}$$

Conversion factors $C_1 and\ C_2\ at\ room\ temperature$ (25 °C) $and\ 1\ atm$

$$C_1 = \frac{44.01 \frac{g}{mol} * \frac{kg}{1000g}}{96485 \frac{C}{mol} \frac{1000mA * s}{C} \frac{h}{3600s} \frac{day}{24hr} \frac{yr}{365day}} \frac{100^2 cm^2}{m^2} = 143.85 \frac{kg}{m^2 * yr} \frac{cm^2}{mA}$$

$$C_2 = \frac{44.01 \frac{g}{mol_{CO_2}} \frac{mol_{CO_2}}{10^6 ppm_{CO_2}} * \frac{kg}{1000g} * \frac{1atm}{1mol_{air} * 298.15K} * \frac{1}{0.082057} * \frac{mol_{air} * K}{L * atm} * \frac{100^2 cm^2}{m^2}}{\frac{hr}{60min} * \frac{day}{24hr} * \frac{yr}{365day}} = 9.454 \frac{kg}{m^2 * yr} \frac{cm^2 * min}{ppm_{CO_2} * L}$$

Variable Definitions:

$j_{stoic_i} = stoichiometric\ flux\ limit\ of\ i$
$j_{massFlow} = mass\ flow\ flux\ limit$
$n_i = moles\ of\ i$
$F = Faraday's\ constant (C \cdot mol^{-1})$

$I = current\ density (mA \cdot cm^{-2})$
$A = electrode\ area (cm^2)$
$m = molar\ mass (g \cdot mol^{-1})$
$Q = Volumetric\ Flow\ Rate\ (L \cdot min^{-1})$

$Subscripts\ i$:
$x = species\ capturing\ CO_2$
$bicarb = bicarbonate$
$carb = carbonate$
$e = electron$
$CO_2 = CO_2$

The 25 cm^2 laboratory cell was held in regeneration at different current densities to observe the constant flux independent of state of charge of the electrodes (**Supplementary Figure 5**). While there is some difference in the maximum flux between the charging and regeneration portions of a cycle, it is a good proxy for the maximum flux at a given current density without effects from the state of charge of the electrodes. The same device as in **Figure 2** of the manuscript was held at 1-5 mA·cm^{-2} for an hour each with an hour relaxation between each hold. The final 5 minutes of the hour were averaged and used as the maximum flux at that current density.

The fluxes from **Supplementary Figure 5** are overlaid onto the data from a hydrogen fuel cell HEMCC in **Supplementary Figure 6.** Both electrochemical devices are bound by the stoichiometric limit of 100% electron efficiency and their respective mass flow limits. The hydrogen fuel cell HEMCC test was conducted at 3 L·min^{-1} while the nickel hydroxide HEMCC was at 2 L·min^{-1}.

Electron efficiencies decrease as the flux approaches mass transport limits. For this reason, the nickel hydroxide cell decreases at lower current densities than the fuel cell device. It shows the importance of

flow rates to performance and highlights future need to pursue improved flow design into these devices to manage higher flow rates.

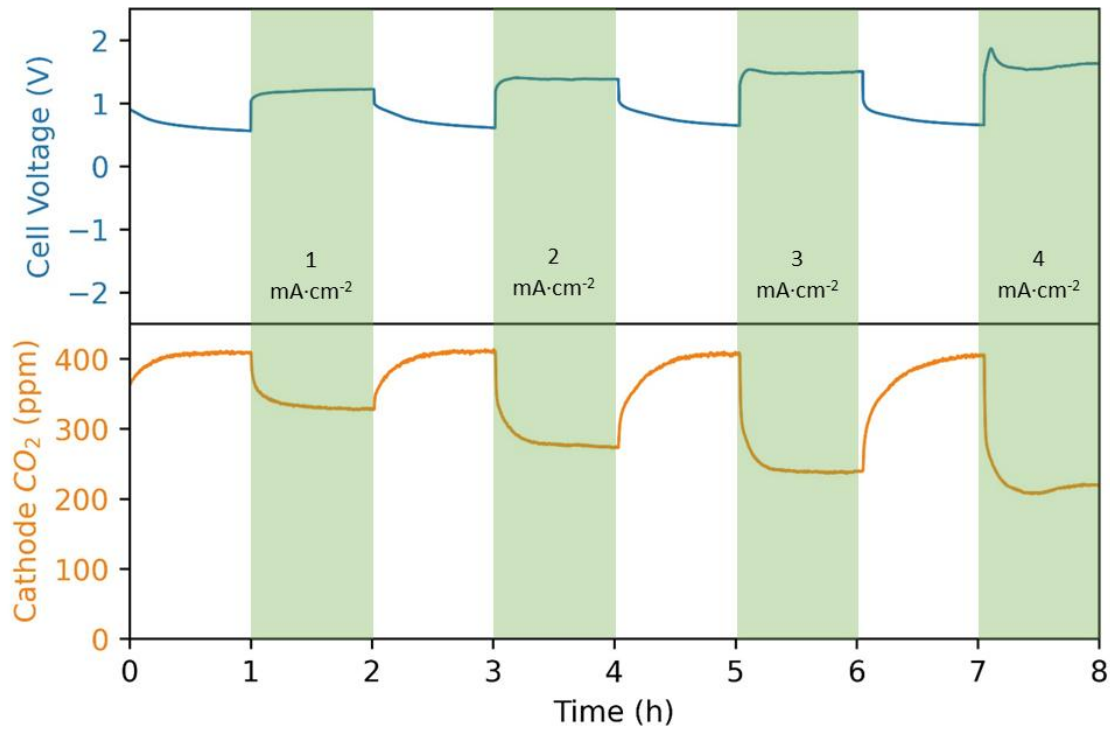

Supplementary Figure 5 | Constant current regeneration flux for maximum flux at different current densities
Voltage and cathode CO2 outlet concentrations for a series of 1 hour rest followed by 1 hour hold at a different current density. The same conditions are used as in Figure 2 of the manuscript. The HEMCC is comprised of two identical electrochemically precipitated Ni(OH)2 electrodes and an 80 µm Piperion® membrane. The cathode air flow was 2 L·min^{-1} with 400 ppm CO2 and 90% RH. The anode received a sweep gas of 90% RH N2 at 2 L·min^{-1}.

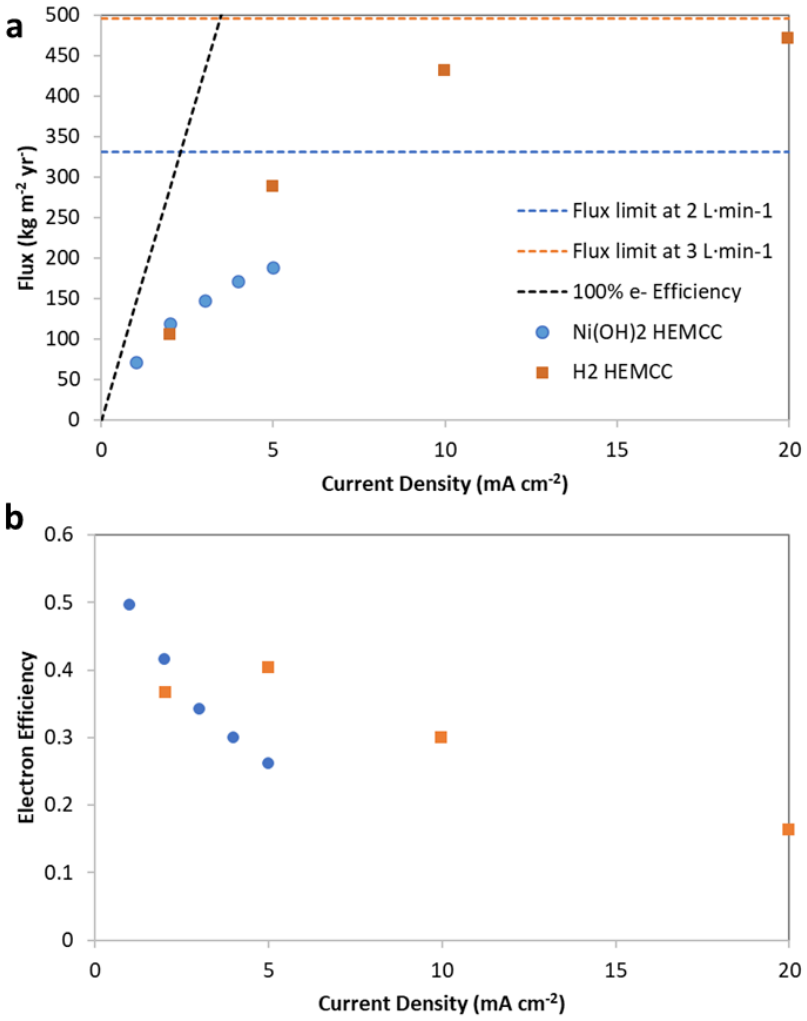

Supplementary Figure 6 | a. Flux b. Electron efficiency vs current density in Ni(OH)2 and H2 fuel cell HEMCC devices
Blue dots are from the regeneration hold in SI Figure 2 while orange are from the H_2 fuel cell presented by Matz et. al 2022. [3] The horizontal dashed lines are maximum fluxes based on mass flow of 400ppm CO_2 with blue 2 L·min-1 for $Ni(OH)_2$ and orange 3 $L \cdot min^{-1}$ for H_2 fuel cell. The dashed black line is the 100% electron efficiency limit. The closer the flux approaches the mass flow limit, the more electron efficiency is bound by that limit instead of electrochemical performance. SI Figure 3a and 3b shares the same legend.

Supplementary Note 5| In-situ corrosion

In both laboratory tests and durability tests, the capacity of the electrodes increased with time. Corrosion of the nickel substrate is the likely reason for this. The durability test showed that the corrosion is limited, and the increased capacity maintains or improves performance of the device. In the manuscript **Figure 3** showed the durability test increased capacity between segment 1 and 2 but not between segment 2 and 3. Similarly, below is a laboratory test of the cell used in **Figure 2** after two additional weeks of testing. The cell is shown performing CO_2 capture from a 400 ppm CO_2 in N_2 stream with a capacity of 2.86 mAh·cm^{-2}. This capacity is greater than ex situ capacity tests of 2.14 and 2.41 mAh cm^{-2} shown in **Supplementary Figure 7** and the reported capacity of 1.89 mAh·cm^{-2} in **Figure 2**. Corrosion of the nickel substrate is a method for increasing the capacity in-situ.

A simplified Pourbaix diagram is shown below in **Supplementary Figure 8** produced from the standard electrochemical reaction potentials of the respective equations. The potential of the cell is always above the nickel corrosion line at $E°_{red}$=0.11V, thus corrosion of the nickel substrate to nickel hydroxide is a possible reaction in the cell. This requires hydroxide to have access to the nickel surface which can be prevented by an oxide or nickel hydroxide layer over the nickel substrate. Hydroxide can still access bare nickel exposed through a crack or uncoated region. Once nickel hydroxide is produced on the nickel surface, a passivation layer of nickel hydroxide prevents further corrosion of the nickel.

To verify that corrosion in the HEMCC requires cycling and that it is likely from the substrate being used, an ex-situ test was set up using the nickel foam substrate to compare corrosion in an electrode held above OER potentials and one that was cycled. A bare 25 cm^2 nickel foam was set in 1 M KOH and held at a current density of 5 mA·cm^{-2} above OER conditions for 400 hours with minimal corrosion evidence shown in **Supplementary Figure 9**.

Another nickel foam substrate was set in 1 M KOH and cycled as if it were a battery in **Supplementary Figure 10**. Charging ended after the electrode stabilized for 20 seconds in OER. Discharge ended at a voltage of 1.1 V vs RHE, with this sample significant corrosion occurred over 16000 cycles. The surface turned physically black and added 16 mg of mass; the capacity of the electrode was 0.055 mAh·cm^{-2}. A mass gain of 16 mg suggests of 43.6 mg of formed $Ni(OH)_2$ which has a theoretical capacity of 0.504 mAh·cm^{-2}.[21]

The difference in corrosion between nickel held in OER vs cycled as a battery shows two things. First, once a passivation layer occurs, corrosion stops and OER becomes the predominant reaction. Second, during a discharge below OER potential, the passivation layer permits transfer of hydroxide to the bare nickel surface. This may occur through α-$Ni(OH)_2$ or γ-NiOOH which allows for ions and small molecules between the layers of the structure.[22] Given that the mass gained during the cycling is significantly higher than what is suggested by the capacity, water and hydroxide have likely filled the space between the $Ni(OH)_2$ layers adding to the mass. Additionally, potassium from the KOH solution can add itself to the nickel structure. The presence of hydroxide in these interstitial layers allows for corrosion to occur when the potential is below OER.

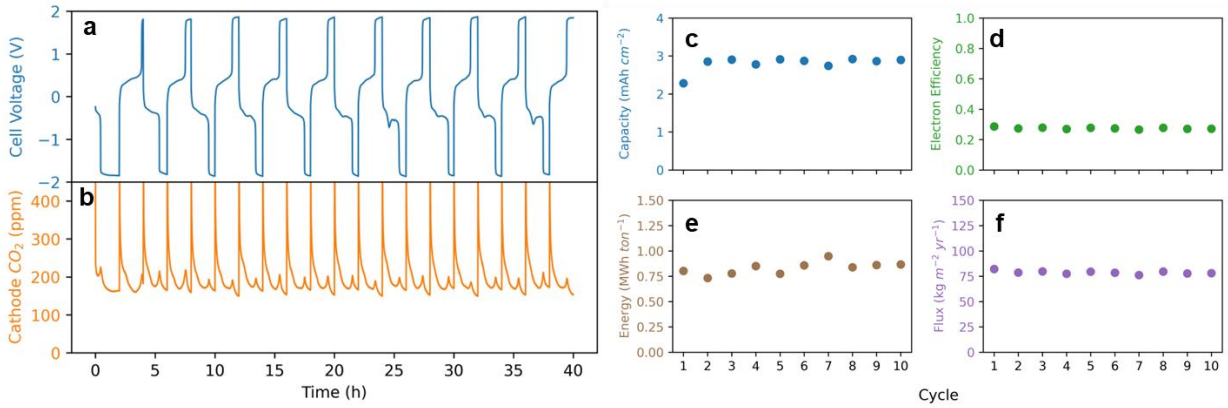

Supplementary Figure 7 | Performance of the laboratory scale HEMCC used in Figure 2 after 2 weeks of additional testing. Including the constant current regeneration tests in **Supplementary Figure 2** The cathode received N_2 flow of 1 L·min^{-1} with 400 ppm CO_2 and 90% RH. The anode received a sweep gas of 90% RH N_2 at 1 L·min^{-1}. The N_2 flow was used to intentionally show a larger voltage during regeneration correlating with HER as the regeneration process instead of ORR when using air. Two-hour cycles were used because of the increased apparent capacity. **a.** The cell voltage (V) and **b.** the cathode outlet CO_2 concentration showed similar behavior as Figure 2 except for higher voltage during regeneration. Key process variables **c-f** during the charge/discharge step **c.** capacity, **d.** electron efficiency, **e.** energy, and **f.** flux. **c.** Capacity was 2.90 mAh·cm^{-2} **d.** Electron efficiency achieved 0.27 **e.** Energy cost averaged 0.83 MWh·ton^{-1} while **f.** Flux averaged to 78 kg·m^2·yr^{-1}.

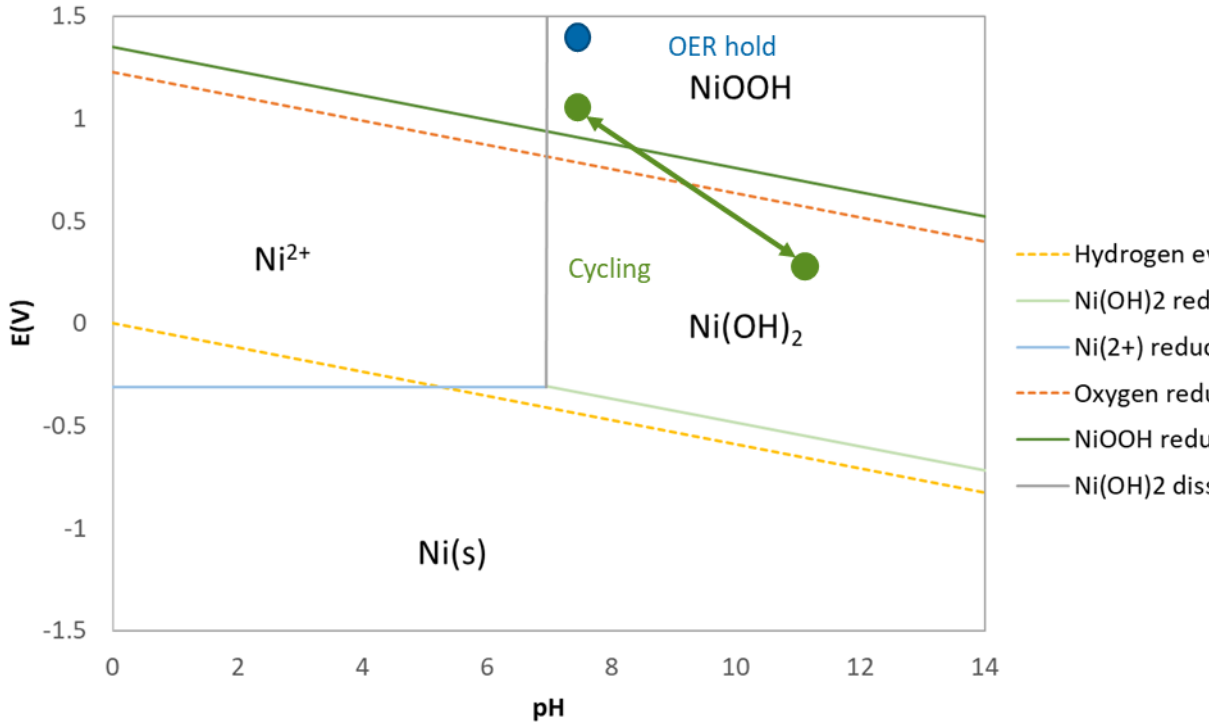

$$\begin{aligned}
&Battery: && NiO(OH) + H_2O + e^- \rightarrow Ni(OH)_2 + OH^- && E^o_{Red} = 1.35V\\
&Electrodeposition: && Ni^{2+} + e^- \rightarrow Ni && E^o_{Red} = -0.31V\\
&Corrosion: && Ni + 2OH^- \rightarrow Ni(OH)_2 + 2e^- && E^o_{Red} = 0.11V\\
&Precipitation: && Ni^{2+} + 2OH^- \rightarrow Ni(OH)_2 &&\\
&Cathode\ (HER): && 2H_2O + 2e^- \rightarrow H_2 + 2OH^- && E^o_{Red} = 0V\\
&Anode\ \ (OER): && 4OH^- \rightarrow 2H_2O + O_2 + 4e^- && E^o_{Red} = 1.23V\\
&Cathode\ (ORR): && 2H_2O + O_2 + 4e^- \rightarrow 4OH^- && E^o_{Red} = 1.23V\\
&Anode\ \ (HOR): && H_2 + 2OH^- \rightarrow 2H_2O + O_2 + 4e^- && E^o_{Red} = 0V
\end{aligned}$$

Supplementary Figure 8 | Simplified Pourbaix diagram for nickel hydroxide.
This is a simplified Pourbaix diagram modified from Huggins.[20] Operation of the cell occurs at high pH and a potential near the OER/ORR line at $E°_{Red}$=1.23V vs RHE. Corrosion of nickel is possible above $E°_{Red}$ =0.11V vs RHE but only in the presence of oxygen. The green dots represent the cycling that occurs in the full cell where CO2 capture occurs at high pH with potentials at or below the OER/ORR line. The blue dot represents a potential hold above OER. In an ex-situ test in SI Figure 7 no corrosion was observed despite potentials sufficiently above the corrosion potential. Relevant electrochemical reactions are shown with their standard reduction potentials.

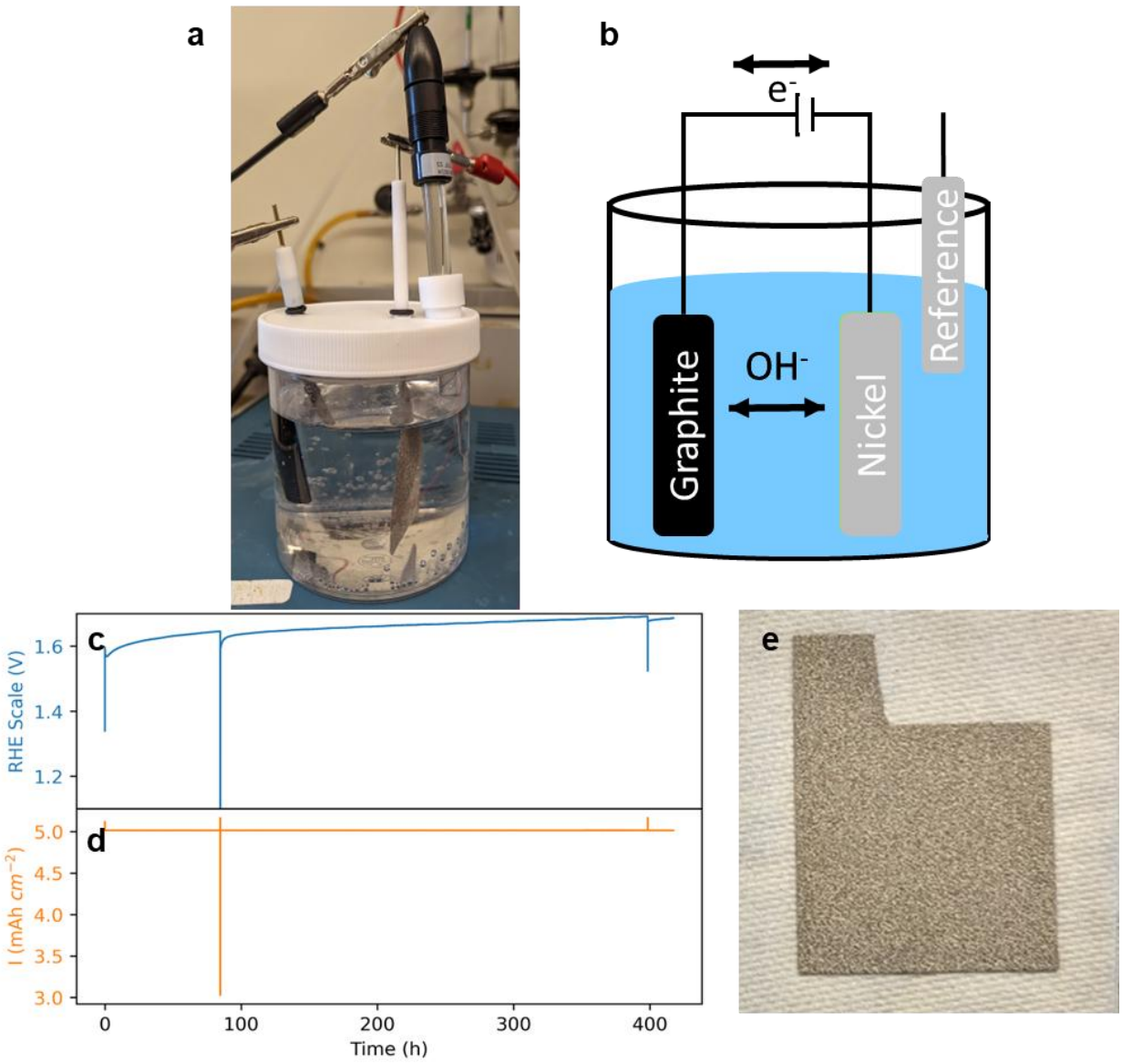

Supplementary Figure 9 | Current density holds to test corrosion on bare nickel foam.
a. Picture of experimental setup with a Ag/AgCl reference, graphite counter electrode, and nickel foam working electrode. **b.** Diagram of picture **c.** Voltage of 25 cm2 nickel foam electrode over 400 hour hold at **d.** 5 mA ·cm-2 current density. There are 2 voltage spikes around 85 hrs and 400 hrs associated with power shut offs and which are not expected to have a large impact on the test. **e.** Picture of the electrode after the current density hold showing little change from the original foam substrate.

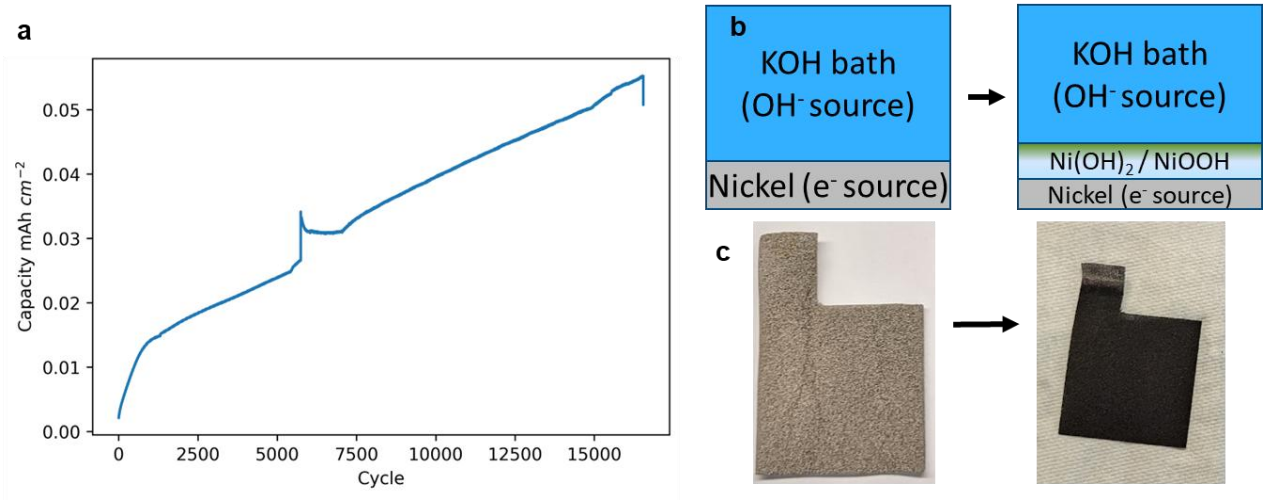

Supplementary Figure 10 | Rapid cycling to test corrosion on bare nickel foam.
A 25 cm^2 nickel foam was placed in 1M KOH and cycled frequently through the $Ni(OH)_2$/NiOOH potential of $E°_{Red}$=1.35V vs RHE**.** Cycling was programed to have the charging end after 20 seconds of stable OER, while the discharge was shut off at a voltage of 1.1 V vs RHE resulting in cycles lasting less than a minute **a.** Capacity of each discharge cycle is shown to show growth of capacity and continued corrosion over time. A power blip mid run caused the spike at 6000 cycles. **b.** Diagram of the conversion of the nickel substrated to nickel with a layer of nickle hydroxide on top of it. **c.** Picture of before and after for this substrate the test showing distinct corrosion covering the entirety of the electrode.

Supplementary Note 6| Laboratory scale pressure drop

Three different flow field arrangements were considered, triple serpentine, single serpentine, interdigitated from Scribner. These are common flow fields used in membrane electrode assembly tests. The triple serpentine has three parallel flow channels passing over the electrode while the single serpentine has only one flow channel at three times the length to cover the same area of the electrode. The interdigitated does not have continues channels and instead has parallel unconnected channels for the inlet and the outlet. This forces the fluid (air) through the electrode and has shorter total path length for the fluid than the serpentine flow fields.

Pressure drop can be modeled using Darcy's law[23] for the triple serpentine and single serpentine configurations as detailed below. The interdigitated has air flow through the electrode substrate and thus is not applicable for Darcy's Law using a channel at a defined length. The results are shown in **Supplementary Figure 11**.

$$\Delta P = f\frac{(L\rho\bar{V}^2)}{2D_H}$$

$$f = \frac{64}{Re}\ for\ laminar\ flow\ Re < 2000\ ; Re = \frac{\rho\bar{V}D_H}{\mu}$$

$$\Delta P\ delta\ pressure\ f = f\frac{(L\rho\bar{V}^2)}{2D_H}$$

$\Delta P = delta\ pressure\ (pressure\ drop)$
$f = friction\ factor$
$L = path\ length$
$\rho = density\ of\ the\ fluid\ (air)$

$\overline{V} = average\ fluid\ velocity$
$D_H = hydrodynamic\ radius$
$Re = Reynold's\ number$
$\mu = kinematic\ viscosity$

At 30°C and 1bar air used in the laboratory cell:

$$\rho_{air} = 1.164\frac{kg}{m^3}; \mu_{air} = 15.98 * 10^{-6}\frac{m^2}{s}$$

For Triple Serpentine Cell at 1 L·min^{-1} flow rate

$$D_H = 8.5 * 10^{-4}m\ (width = 7.5 * 10^{-4}m; depth = 1 * 10^{-3}m);\ L = 0.55m; \bar{V} = 7.4\ m \cdot s^{-1}$$

$$\Delta p = 3300\ Pa; Re = 397$$

For Single Serpentine Cell at 1 L·min^{-1} flow rate.

$$D_H = 8.5 * 10^{-4}m\ (width = 7.5 * 10^{-4}m; depth = 1 * 10^{-3}m);\ L = 1.7m; \bar{V} = 22.2\ m \cdot s^{-1}$$

$$\Delta p = 29700\ Pa; Re = 1190$$

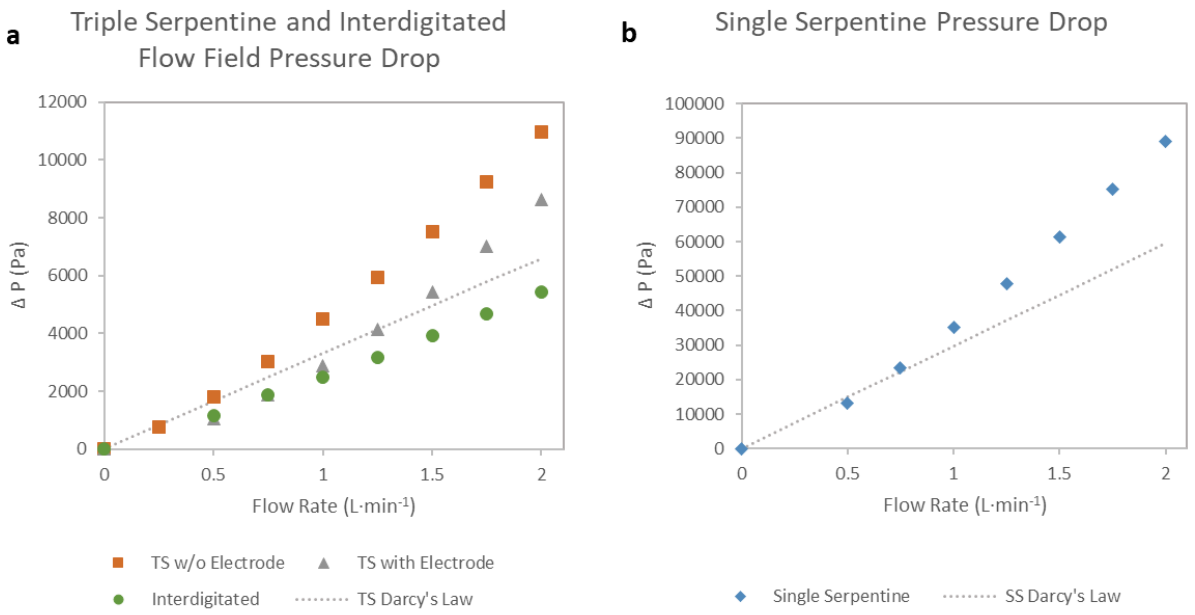

Supplementary Figure 11 | Laboratory scale pressure drop of three different flow field types and 0-2 L·min^{-1} flow rate. **a.** Pressure drop in triple serpentine and interdigitated flow fields. Orange square dots are for a triple serpentine flow field with a gasket in place of an electrode. This has a higher-pressure drop than a triple serpentine flow field with an electrode (grey triangles) due to gas flow through the electrode itself lowering the pressure drop. The linear dotted line represents Darcy's Law approximation of the pressure drop in the flow field. Interdigitated flow is shown on this figure as a comparison to the triple serpentine flow fields. **b.** Pressure drop in a single serpentine flow field (blue diamonds) and the Darcy's Law approximation.

The triple serpentine flow field was chosen in the laboratory setting for having a modest pressure drop while maintaining good performance. A cell with a gasket in place of the electrode was used to compare against Darcy's Law. The actual pressure drop of the triple serpentine flow field is higher than Darcy's law due to added friction factor from turns within the cell as well as the inlet and outlet 1/8th NPT inch Swagelok connectors to the flow field. When the cell was tested with the electrode the pressure drop decreases as there is flow allowed through the electrode in addition to the channel.

The lowest pressure drop is seen with the interdigitated flow field where the entirety of the flow is pushed through the 330 µm electrode. The largest pressure drop is seen with the single serpentine flow field which has three times the path length and three times the velocity of the triple serpentine flow field. Of minor note, the Reynolds number for the single serpentine flow field does slightly exceed the limit defined for laminar flow above 1.75 L·min^{-1}.

Supplementary Note 7| TEA Analysis

A techno-economic analysis was developed and conducted based on previously reported models. [2,24]

1. Active area

The analysis considers five different projects over a 20-year operating period designed around the following nameplate capacities: 1 $kton_{CO2}·yr^{-1}$, 10 $kton_{CO2}·yr^{-1}$, 100 $kton_{CO2}·yr^{-1}$, 1000 $kton_{CO2}·yr^{-1}$ First of a Kind (FOAK), 1000 $kton_{CO2}·yr^{-1}$ Nth of a Kind (NOAK). A capacity factor of 95% and a net negativity (net/gross ratio) of 92% are assumed.

An improvement of the CO_2 flux is considered with the increase of nameplate capacity, in line with a progressive maturation of the technology (theoretical limits and approaches for achieving performance improvements are described in **Supplementary Note 4** and the main manuscript, respectively):

Nameplate capacity ($kton_{CO2}·yr^{-1}$)	**1**	**10**	**100**	**1000 FOAK**	**1000 NOAK**
CO_2 flux ($kg_{CO2}·m^2·yr^{-1}$)	100	200	200	300	300
Active area (m^2)	10000	50000	500000	3333333	3333333

$$Active\ area = \frac{Nameplate\ capacity * 1000000}{CO_2\ flux}$$

2. Capex

A Bill Of Material (BOM) was established as a comprehensive list of raw materials, components, sub-assemblies, and parts required to manufacture and assemble the stacks of cells. Three different factories are considered:

	Automated factory	**Megafactory**	**Gigafactory**
Produced active area ($m^2.y^{-1}$)	500000	5000000	40000000
Assembled stacks ($\#.y^{-1}$)	10000	100000	800000
Investment cost ($)	45000000	283000000	1423000000
Depreciation (y)	10	10	10
COGS ($.m^{-2}$)	200	170	130
Unit cost ($.m^{-2}$)	209	176	134

$$Unit\ cost = COGS + \frac{Investment\ cost / Depreciation}{Produced\ active\ area}$$

The Bare Erected Cost (BEC) can be derived from the Unit cost and the Active area. It comprises the cost of core process equipment, on-site facilities, and auxiliary systems.

Nameplate capacity ($kton_{CO2}·yr^{-1}$)	**1**	**10**	**100**	**1000 FOAK**	**1000 NOAK**
Active area (m^2)	10000	50000	500000	3333333	3333333
Unit cost ($.m^{-2}$)	209	209	176	176	134
BEC (k$)	2090	10450	88000	586667	446667

$$Bare\ Erected\ Cost = \frac{Unit\ cost * Active\ area}{1000}$$

The Total Plant Cost (TPC) encompasses the Engineering, Procurement, and Construction (EPC) costs, along with process and project contingencies. The EPC costs cover services provided by the contractor, including detailed design, contractor permitting, and project/construction management. Process contingencies account for uncertainties in cost estimates arising from performance risks associated with the technology's development status. Project contingencies address general uncertainties in cost estimates and potential risks related to the plant's overall development.

Nameplate capacity ($kton_{CO2} \cdot yr^{-1}$)	**1**	**10**	**100**	**1000 FOAK**	**1000 NOAK**
BEC (k$)	2090	10450	88000	586667	446667
EPC factor (%)	20%	20%	20%	20%	20%
Process contingencies (%)	20%	20%	10%	5%	5%
Project contingencies (%)	20%	20%	15%	10%	10%
TPC (k$)	3612	18058	133584	813120	619080

$$Total\ Plant\ Cost = BEC * (1 + EPC\ factor) * (1 + Process\ contingencies) * (1 + Project\ contingencies)$$

The Total Overnight Capital (TOC) comprises the TPC plus the owner's costs.

Nameplate capacity ($kton_{CO2} \cdot yr^{-1}$)	**1**	**10**	**100**	**1000 FOAK**	**1000 NOAK**
TPC (k$)	3612	18058	133584	813120	619080
Owner's cost factor (%)	7%	7%	7%	7%	7%
TOC (k$)	3865	19322	142935	870038	662416

$$Total\ Overnight\ Capital = TPC * (1 + Owner's\ cost\ factor)$$

BEC, TPC and TOC are expressed in base-year dollars.

3. Opex

Fixed Operation & Maintenance (O&M) costs include recurring O&M material costs, labor, insurance and land rental:

- Yearly recurring O&M material costs are assumed to be 1.5% of the TOC.
- Regarding labor, while the number of operators, supervisors, and maintenance workers is usually constant for a given process, the labor rate and burden can vary widely between locations. The analysis considers an average Total Cost Of Employment (TCOE) of K$50 per Full Time Employee (FTE) as well as an additional management fee of 10%.
- Insurance costs are assumed to be 0.5% of the TOC.
- Land rental costs are adjusted to the footprint of each projects

Nameplate capacity ($kton_{CO2} \cdot yr^{-1}$)	**1**	**10**	**100**	**1000 FOAK**	**1000 NOAK**
O&M material ($k\$ \cdot yr^{-1}$)	58	290	2144	13051	9936
Labor (FTE)	2	10	20	40	40
Labor ($k\$ \cdot yr^{-1}$)	110	550	1100	2200	2200

Insurance (k$·yr^{-1})	19	97	715	4350	3312
Land rental (k$·yr^{-1})	20	150	300	1000	1000
TFOM (k$·yr^{-1})	207	1087	4259	20601	16448

$$TFOM = O\&M\ material + Labor + Insurance + Land\ rental$$
$$= 1.5\% * TOC + FTE * TCOE * (1 + 10\%) + 0.5\% * TOC + Land\ rental$$

Variable O&M costs include purchased power and replacement of core electrochemical units:

- Purchased power:
  - Power consumption
    - Core electrochemical units – calculations of flux and energy cost are shown in **Supplementary Note 2**. Energy consumption decreases with increasing technology maturity due to improvements in electrode formulation and morphology as well as stack design. Both aspects contribute to improved electrical and ion conductivity, charge capacity and mass transport (diffusion), eventually leading to increased CO_2 flux and increased %removal of the CO_2 in the air stream.
    - Periphery – the main drivers are the Air Supply Unit (ASU) elements: axial fan and humidifier. Assuming ambient conditions of T=10-40°C and RH=75-95%, a humidifier to top up water vapor is neglected. The energy consumption of the fan is expected to drop due to improvements in the following aspects: (1) improved CO_2 flux, as described above. (2) improved stack design, reducing pressure drop to a target of ~100 Pa. (3) Scaling up and centralization of ASU feeding multiple stacks, leading to improved energy efficiency.
  - Electricity price is considered at 5 cent/kWh
- Replacement of core electrochemical units: frequency of replacement increasing from 10 years to 20 years with increasing technology maturity. Such lifetime is reasonable to assume considering the main MEA components:
  - Nickel hydroxide based electrodes have been comprehensively researched and utilized in Ni-MH and Ni-Cd batteries over the last few decades, reaching 15+ years of operation.
  - AEM – lifetime of 5,000-10,000 hours have been reported in other applications (e.g. fuel cells, electrolyzers) operating at higher temperatures (90-100°C) and current densities (>1 A.cm^{-2}). Considering milder process conditions (10-40°C, 1-5 mA.cm^{-2}), orders of magnitude increase of the membrane lifetime is expected. [25]

Nameplate capacity (kton$_{CO2}$·yr^{-1})	**1**	**10**	**100**	**1000 $_{FOAK}$**	**1000 $_{NOAK}$**
Power consumption (kWh.t$_{CO2}^{-1}$)	1200	1000	800	650	650
Electricity price ($.kWh^{-1})	0.05	0.05	0.05	0.05	0.05
Purchased power ($·t$_{CO2}^{-1}$)	60	50	40	33	33
Purchased power (k$·yr^{-1})	57	475	3800	30875	30875
Core units replacement (year)	10	10	10	20	20
Replacement cost (k$)	754	5029	27351	0	0
Annualized replacement (k$·yr^{-1})	38	251	1368	0	0

TVOM (k$·yr^{-1})	95	726	5168	30875	30875

$$TVOM = Purchased\ power + Annualized\ replacement$$
$$= Power\ consumption * Electricity\ price * Nameplate\ capacity * 1000 * Capacity\ factor + {}^{Replacement\ cost}/_{Operating\ Period}$$

4. Levelized Cost of Capture (LCOC)

The LCOC can be calculated by summing the annualized total capital, the annual fixed O&M costs, the annual variable O&M costs (including annualized replacement costs) and dividing by the annual net carbon captured.

$$LCOC = \frac{{}^{TOC}/_{OP} + TFOM + TVOM}{Nameplate\ capacity * Capacity\ factor * {}^{Net}/_{Gross}\ ratio}$$

where:

- LCOC – levelized cost of capture, $. t $_{CO2}^{-1}$
- TOC – total overnight cost, k$
- OP – operating period, years
- TFOM – total annual fixed O&M, $·yr^{-1}
- TVOM – total annual variable O&M, $·yr^{-1}
- Nameplate capacity – total annual gross CO_2 captured, kt$_{CO2}$·yr^{-1}
- Capacity factor – yearly average plant availability, fraction
- Net/Gross ratio – net negativity, fraction

Nameplate capacity (kton$_{CO2}$·yr^{-1})	**1**	**10**	**100**	**1000 $_{FOAK}$**	**1000 $_{NOAK}$**
LCOC ($·t$_{CO2}^{-1}$)	566	318	190	109	92

This TEA assumes an energy price of 0.05 MWh·ton$_{CO2}^{-1}$ for the NOAK capture cost to reach 92 $·ton$_{CO2}^{-1}$. A sensitivity to this energy is shown below.

Energy price ($·MWh)	**0.03**	**0.05**	**0.07**
NOAK capture cost ($·ton$_{CO2}^{-1}$)	78	92	106

Supplementary Figure 12 | RepAir Direct Air Capture Pilot Ni(OH)2 HEMCC.

Supplementary References

1 House, K. Z. *et al.* Economic and energetic analysis of capturing CO2 from ambient air. *Proc Natl Acad Sci U S A* **108**, 20428-20433 (2011). https://doi.org:10.1073/pnas.1012253108

2 Zhu, P. *et al.* Continuous carbon capture in an electrochemical solid-electrolyte reactor. *Nature* **618**, 959-966 (2023). https://doi.org:10.1038/s41586-023-06060-1

3 Matz, S. *et al.* Hydrogen-powered Electrochemically-driven CO2 Removal from Air Containing 400 to 5000 ppm CO2. *Journal of The Electrochemical Society* **169** (2022). https://doi.org:10.1149/1945-7111/ac7adf

4 Seo, H. & Hatton, T. A. Electrochemical direct air capture of CO(2) using neutral red as reversible redox-active material. *Nat Commun* **14**, 313 (2023). https://doi.org:10.1038/s41467-023-35866-w

5 Wang, M., Herzog, H. J. & Hatton, T. A. CO2 Capture Using Electrochemically Mediated Amine Regeneration. *Industrial & Engineering Chemistry Research* **59**, 7087-7096 (2020). https://doi.org:10.1021/acs.iecr.9b05307

6 Li, X. *et al.* Redox-tunable isoindigos for electrochemically mediated carbon capture. *Nat Commun* **15**, 1175 (2024). https://doi.org:10.1038/s41467-024-45410-z

7 Diederichsen, K. M., Liu, Y., Ozbek, N., Seo, H. & Hatton, T. A. Toward solvent-free continuous-flow electrochemically mediated carbon capture with high-concentration liquid quinone chemistry. *Joule* **6**, 221-239 (2022). https://doi.org:10.1016/j.joule.2021.12.001

8 Iizuka, A. *et al.* Carbon dioxide recovery from carbonate solutions using bipolar membrane electrodialysis. *Sep. Purif. Technol.* **101**, 49-59 (2012). https://doi.org:10.1016/j.seppur.2012.09.016

9 Eisaman, M. D. *et al.* CO2 separation using bipolar membrane electrodialysis. *Energy Environ. Sci.* **4**, 1319-1328 (2011). https://doi.org:10.1039/c0ee00303d

10 Keith, D. W., Holmes, G., St. Angelo, D. & Heidel, K. A Process for Capturing CO2 from the Atmosphere. *Joule* **2**, 1573-1594 (2018). https://doi.org:10.1016/j.joule.2018.05.006

11 McQueen, N. *et al.* A review of direct air capture (DAC): scaling up commercial technologies and innovating for the future. *Progress in Energy* **3** (2021). https://doi.org:10.1088/2516-1083/abf1ce

12 Chen, Y. & Kanan, M. W. Thermal Ca(2+)/Mg(2+) exchange reactions to synthesize CO(2) removal materials. *Nature* **638**, 972-979 (2025). https://doi.org:10.1038/s41586-024-08499-2

13 Mukherjee, S. *et al.* Trace CO(2) capture by an ultramicroporous physisorbent with low water affinity. *Sci Adv* **5**, eaax9171 (2019). https://doi.org:10.1126/sciadv.aax9171

14 Wang, X., Conway, W., Burns, R., McCann, N. & Maeder, M. Comprehensive Study of the Hydration and Dehydration Reactions of Carbon Dioxide in Aqueous Solution. *The Journal of Physical Chemistry A* **114**, 1734-1740 (2010). https://doi.org:10.1021/jp909019u

15 Shu, Q., Legrand, L., Kuntke, P., Tedesco, M. & Hamelers, H. V. M. Electrochemical Regeneration of Spent Alkaline Absorbent from Direct Air Capture. *Environ Sci Technol* **54**, 8990-8998 (2020). https://doi.org:10.1021/acs.est.0c01977

16 Cadogan, S. P., Maitland, G. C. & Trusler, J. P. M. Diffusion Coefficients of CO2 and N2 in Water at Temperatures between 298.15 K and 423.15 K at Pressures up to 45 MPa. *Journal of Chemical & Engineering Data* **59**, 519-525 (2014). https://doi.org:10.1021/je401008s

17 Carroll, J. J. S., J. D.; Mather, A. E. The Solubility of Carbon Dioxide in Water at Low Pressure. *J. Phys. Chem. Ref. Data.* **20** (1991).

18 Bandura, V. A. L., N. S. The Ionization Constant of Water over Wide Ranges of Temperature and Density. *J. Phys. Chem. Ref. Data.* **35** (2006). https://doi.org:10.1063/1.1928231

19 Luo, X., Rojas-Carbonell, S., Yan, Y. & Kusoglu, A. Structure-transport relationships of poly(aryl piperidinium) anion-exchange membranes: Eeffect of anions and hydration. *Journal of Membrane Science* **598** (2020). https://doi.org:10.1016/j.memsci.2019.117680

20 Huggins, R. A. *Advanced Batteries Materials Science Aspects*. 216-234 (Springer, 2009).

21 Ash, B., Nalajala, V. S., Popuri, A. K., Subbaiah, T. & Minakshi, M. Perspectives on Nickel Hydroxide Electrodes Suitable for Rechargeable Batteries: Electrolytic vs. Chemical Synthesis Routes. *Nanomaterials (Basel)* **10** (2020). https://doi.org:10.3390/nano10091878

22 Hall, D. S., Lockwood, D. J., Bock, C. & MacDougall, B. R. Nickel hydroxides and related materials: a review of their structures, synthesis and properties. *Proc Math Phys Eng Sci* **471**, 20140792 (2015). https://doi.org:10.1098/rspa.2014.0792

23 Barbir, F., Gorgun, H. & Wang, X. Relationship between pressure drop and cell resistance as a diagnostic tool for PEM fuel cells. *Journal of Power Sources* **141**, 96-101 (2005). https://doi.org:10.1016/j.jpowsour.2004.08.055

24 Henry, S. *et al.* Basis for techno-economic analysis carbon utilization procurement grants. (United States Department of Energy National Energy Technology Laboratory, 2023). <https://netl.doe.gov/sites/default/files/2023-03/BIL%20FOA%202829%20-%20Basis%20for%20Techno-Economic%20Analysis%202023_01_30.pdf>

25 Moreno-González, M. *et al.* One year operation of an anion exchange membrane water electrolyzer utilizing Aemion+® membrane: Minimal degradation, low H2 crossover and high efficiency. *Journal of Power Sources Advances* **19** (2023). https://doi.org:10.1016/j.powera.2023.100109